Ceramics International 49 (2023) 23391–23398

Contents lists available at ScienceDirect

Ceramics International

journal homepage: www.elsevier.com/locate/ceramint

Defect-engineered hexagonal boron nitride nanosheets as a new atomic-level directional ion conductor

Guoqing Wang [a], Xiaoyan Luo [a], Chen Chen [a], Birkneh Sirak Teketel [a], Bo Xu [b], Weili Yu [c], Bin Lin [a,*]

[a] School of Mechanical and Electrical Engineering, University of Electronic Science and Technology of China, Chengdu, 611731, PR China
[b] Department of Physics, Laboratory of Computational Materials Physics, Jiangxi Normal University, Nanchang, 330022, PR China
[c] GPL Photonics Laboratory, State Key Laboratory of Luminescence and Applications, Changchun Institute of Optics, Fine Mechanics and Physics, Chinese Academy of Science, Changchun, Jilin, 130033, PR China

ARTICLE INFO

Handling Editor: Dr P. Vincenzini

Keywords:
Hexagonal boron nitride
Vacancy defects
Directional control
Atomic-level directional ion conductor
Bioinspired nanofluidic iontronic devices

ABSTRACT

With electron-conducting information technology, ion-conducting energy and environmental technology are promising for wide applications in a carbon-neutral world, but it has been challenging to achieve directional ion conduction in fast ion conductors, especially at the microscopic or even atomic scale. Here, the authors report a new atomic-level directional ion conductor of defect-engineered hexagonal boron nitride (*h*-BN) nanosheets for bioinspired nanofluidic iontronic devices, and propose a vacancy-defect-controlled strategy to achieve atomic-level directional hydrogen ion conduction in *h*-BN nanosheets. The adsorption and migration behaviors of hydrogen ions in *h*-BN nanosheets with both B and N vacancy defects were systematically investigated through the first-principle method. The best hydrogen adsorption sites are directly above N and B atoms in the B-vacancy and N-vacancy *h*-BN, respectively. It is found that the migration barriers of hydrogen ion in B-vacancy and N-vacancy *h*-BN are as high as 1.83–2.47 eV and 1.71–2.30 eV, respectively, which are much higher than the 0.72 eV of intrinsic *h*-BN nanosheets. This means that hydrogen ions can conduct in defect-free *h*-BN, while they cannot conduct in B/N-vacancy defects. Accordingly, hydrogen ion conduction in *h*-BN nanosheets can be directionally controlled by controlling the position of vacancy defects, which can be artificially constructed by femtosecond laser plasma lithography. This work provides a new technology of vacancy-defect-controlled atomic-level directional ions conduction in 2D materials for ion-conductor integrated circuit, and opens the door for constructing bioinspired nanofluidic iontronic devices in future neuronal-computer interfaces.

1. Introduction

Ion conductors are of great essential in the fields of energy [1–4], sensors [5–9], artificial intelligence [10–13], and so on. Hydrogen/oxygen-ion conduction and lithium-ion conduction are the cores of fuel cells and lithium-ion batteries, respectively. Walther Nernst [14] first discovered that yttrium-stabilized zirconia (YSZ) can be used as an oxygen-ion conductor, opening the door to solid-state ionic devices. Additionally, Hiroyasu Iwahara et al. [15] were surprised to find proton conduction in doped $SrCeO_3$ perovskite oxides and began developing protonic ceramic devices. In 2019, John B. Goodenough [16,17] won the Nobel Prize in recognition of his outstanding contributions to the field of lithium-ion batteries. For sensors, hydrogen sensors are common [18–21]. Zhi et al. [21] prepared the Pt/C/Nafion film and applied it to the hydrogen sensor. Hydrogen molecules are decomposed into hydrogen ions due to the catalysis of platinum (Pt), while Nafion has a high conductivity of protons. The sensitivity of the sensor is greatly improved by this electrochemical behavior. For artificial intelligence, the emergence of ionics, which realizes the organic combination of ion transmission and conductivity, will become the most potential signal transmission medium between electronic devices and biological systems, and establish a bridge between biological brain and artificial brain [22–24]. Tan et al. [25] used the migration of ionic defects (oxygen vacancies, protons) in oxides to develop volatile adjustable memristive devices, and successfully simulated the function of biological synapses to realize the dynamic recognition of moving objects. Hou et al. [26] believes that nanofluidic-ion devices based on ion conduction will be the most likely development direction to realize the two-way connection

* Corresponding author.
E-mail address: bin@uestc.edu.cn (B. Lin).

https://doi.org/10.1016/j.ceramint.2023.04.171
Received 12 February 2023; Received in revised form 11 April 2023; Accepted 23 April 2023
Available online 24 April 2023

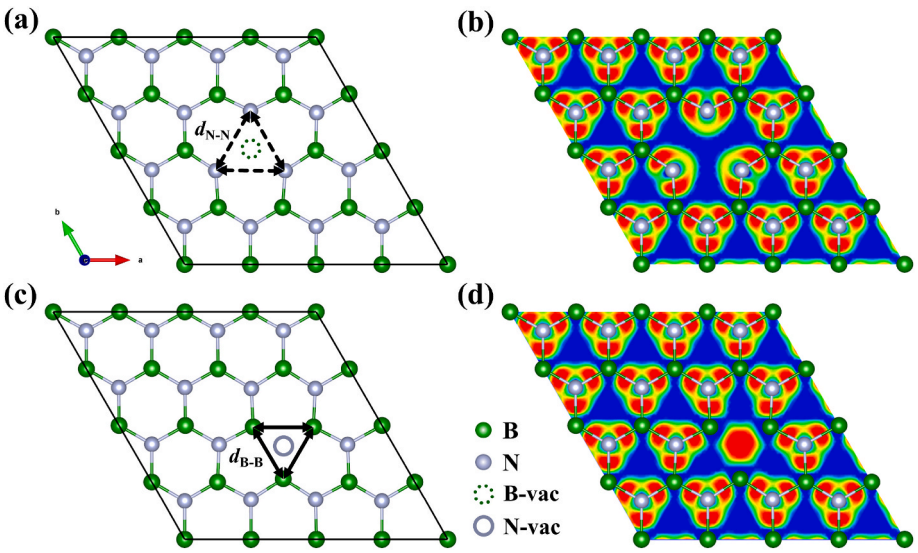

Fig. 1. The structure of (a) V_B *h*-BN nanosheets and (c) V_N *h*-BN nanosheets. Green balls represent the B element and grey balls represent the N element; the green dashed circle represents V_B and the grey solid circle represents V_N. The sliced ELF map of (b) V_B *h*-BN nanosheets and (d) V_N *h*-BN nanosheets on the (001) crystal face. (For interpretation of the references to colour in this figure legend, the reader is referred to the Web version of this article.)

between the brain and computer. As we know, there is the essential difference between computers and biological systems [26]. The conventional computer with intensive energy consumption is of electron conduction with the aim to decrease device sizes in integrated circuits, while the biological system with energy-efficient characteristic ionic signals is of ion conduction with the aim to achieve sophisticated control of ions in different materials and to interface with biological processes. With the combination of electron and ion conductions, nanofluidic iontronic devices are for signal processing and are promising to develop future neuronal-computer interfaces [27].

Ion conduction is ubiquitous in all types of materials. According to the structural characteristics of different dimensions, it can be divided into zero-dimensional (0-D), one-dimensional (1-D), two-dimensional (2-D), and three-dimensional (3-D) materials. There are many types of 0-D materials, including quantum dots, clusters, nano cages, core-shell structures and so forth [28,29]. Sun et al. [30] successfully synthesized the cubic anti-perovskite Na_3OBH_4 material. Through neutron diffraction experiments, it was found that the BH_4 cluster in Na_3OBH_4 can rotate freely; moreover, the rotation of the BH_4 cluster can promote the conduction of Na^+ ions. Zhu et al. [31] used 1 MeV Ne^{8+} ions to collide with the neutral N_2Ar cluster, and observed strange heavy N^+ ion transfer channel. 1-D materials include nanotubes, nanorods, nanowires and nanoribbons. Among them, carbon nanotube (CNT) [32] is representative of 1-D materials. Liu et al. [33] successfully prepared a carbon nanotube-based mesoporous material with an impregnation of red P, and demonstrated its high Na^+ or K^+ storage capacity, ultrafast ion conduction rate, as well as, outstanding ion cycle stability. Won et al. [34] studied the selective permeability of boron nitride nanotubes to KCl solution by density functional theory and molecular dynamics simulation, showing that only Cl^- ions can conduct and transport in the boron nitride nanotube. 2-D materials [35,36] refer to materials in which electrons can only move freely on the nanoscale of two dimensions (plane motion), such as nanofilms, nanosheets, and superlattices, etc. Yoo et al. [37] researched the lithium storage performance of graphene nanosheets as a high-capacity cathode material for rechargeable lithium-ion batteries. They found that the specific capacity of graphene nanosheets is 540 mAh/g, which is much larger than that of graphite 372 mAh/g. Hatakeyama et al. [38] prepared composite films by introducing sulfate ions into the intermediate layer of graphene oxide, showing high proton conductivity. 3D materials have a highly specific surface area, interconnected porous channels, high conductivity, and excellent structural stability [39,40]. Most fast ionic conductors are 3D materials [14,17,41–46]. So far, the studies on ion conduction in materials with different dimensions still stay in meso- or macro-scale measurement, and remain huge challenges to the achievement of atomic-scale control, especially for the ideal atomic-level directional ions conduction.

Hexagonal boron nitride (*h*-BN) [47], also known as “white graphene”, is the lightest and most important III-V group material. It has many unique characteristics, including high mechanical strength [48], good thermal conductivity [49], high melting point [50], and simple preparation [51]. Furthermore, *h*-BN nanosheets has good proton penetration properties. Hu et al. [52] proved through experiments that at room temperature, a proton can penetrate the complete structure of the monolayer *h*-BN, as well as, the conductivity is 100 mS/cm^2 and the low activation energy is ~0.3 eV. Moreover, our previous work systematically studied the influence of tensile strain on the transport behavior of hydrogen ions at the surface of pure *h*-BN [53]. In the process of preparing *h*-BN experimentally, there are always intrinsic vacancies, including B atom vacancies (V_B) and N atom vacancies (V_N) [54–56]. Peng et al. [57] reviewed the impact of defect-engineering on the *h*-BN and discovered the changes in exotic characteristics brought about by defect-engineering. Zhang et al. [58] theoretically studied the mechanism of methane dry reforming reactions over *h*-BN nanosheets supporting Ni catalysts by means of density functional theory. They found that compared with intact *h*-BN nanosheets, B-vacancies *h*-BN exhibited better metal-carrier interaction properties with Ni and were able to promote the methane dry reforming reaction. Shen et al. [59] revealed the complex mechanical response of *h*-BN containing vacancy defects through extensive molecular dynamics simulations. And besides, a machine learning model based on convolutional neural networks has been established to effectively predict the mechanical properties of the vacancy *h*-BN.

In this work, by introducing V_B and V_N into *h*-BN nanosheets and choosing hydrogen ions as the proof of concept, we develop a new method to achieve controllable directional conduction of hydrogen ion at the atomic-scale for the first time. The first-principle calculation results show that the migration barrier of hydrogen ions on the intrinsic *h*-BN surface is much lower than that on the *h*-BN with vacancy defects, proving that the existence of vacancies affects and changes the migration path of hydrogen ions in *h*-BN. The vacancy defects can be artificially introduced into *h*-BN nanosheets, so the directional conduction of

Table 1
Lattice constant a and b (Å), lattice angle α, β and γ (°), bond length $d_{B\text{-}B}$ and $d_{N\text{-}N}$ (Å), and the number of B/N atoms (B_{AN}/N_{AN}) of different configurations BN.

sample	$a = b$	$\alpha = \beta$	γ	$d_{B\text{-}B}$	$d_{N\text{-}N}$	B_{AN}	N_{AN}
h-BN	10.00	90	120	2.50	2.50	16	16
B-vacancy	9.99	90	120	–	2.64	15	16
N-vacancy	9.89	90	120	2.21	–	16	15

hydrogen ions can be artificially controlled.

2. Experimental

This practical work applied a first-principle method based on the density functional theory [60,61], using a current software of the Vienna *ab-initio* Simulation Package (VASP) [62–64]. The interaction between valence electrons and ionic reals is represented by the projected-augmented wave pseudopotential [65]. The exchange correlation potential adopts Perdew-Burke-Ernzerhof under generalized-gradient approximation [66]. The cut-off energy was 400 eV. The integration of Brillouin zone adopts the Monkhorst-Pack method [67]. The *k*-points mesh of 3 × 3 × 1 for unit cell was utilized in the structural optimization, and the 5 × 5 × 1 was utilized in the electronic properties. The energy of convergence criterion was $\leq 10^{-5}$ eV, and the Hellman-Feynman force acting on each atom was ≤0.005 eV/Å. To eliminate the interaction between B-vacancy (V_B) and N-vacancy (V_N) *h*-BN nanosheets, a vacuum layer of 15 Å was selected in the direction perpendicular to the *h*-BN plane. The van der Waals interaction correction (DFT-D2) was used [68,69]. The climbing-image nudged elastic band [70] was applied to determine the hydrogen ion transport path and the energy barrier, and the VESTA drawing software [71] is used.

Ordinarily, the adsorption energy E_{ad} is important for comprehending the hydrogen ion adsorption behavior on the V_B/V_N *h*-BN nanosheets surface. A negative value means hydrogen ions can be adsorbed on the V_B/V_N *h*-BN surface. Here, the E_{ad} is defined as follows:

$$E_{ad} = E_{VB/VN\ h-BN+H} - E_{VB/VN\ h-BN} - E_H \quad (1)$$

where $E_{VB/VN\ h\text{-}BN+H}$ and $E_{VB/VN\ h\text{-}BN}$ are the optimized total ground state energies of the V_B/V_N *h*-BN with hydrogen and V_B/V_N *h*-BN nanosheets, respectively. E_H is the total energy of an isolated hydrogen atom.

3. Results and discussion

3.1. The structure and electronic properties of V_B and V_N h-BN nanosheets

As shown in Fig. 1, we first discussed the structural properties of B-vacancy (V_B) and N-vacancy (V_N) *h*-BN nanosheets. The geometrically optimized lattice constants a and b, lattice angles α, β and γ, B–B bond lengths $d_{B\text{-}B}$, N–N bond lengths $d_{N\text{-}N}$, and the number of B/N atoms are listed in Table 1. Fig. 1(a) shows the structure of the V_B *h*-BN nanosheets. The lattice constant is $a = b = 9.99$ Å, lattice angle $\alpha = \beta = 90°$ and $\gamma = 120°$, and bond length $d_{N\text{-}N} = 2.64$ Å. The number of B atoms in the V_B *h*-BN primitive cell is 15 and the number of N atoms is 16. Moreover, the electron localization function (ELF) map of V_B *h*-BN nanosheets is shown in Fig. 1(b), which can provide a clear image of the charge localization. According to Fig. 1(b), no charge was localized at the B-vacancy, and the charge was mainly distributed on the B–N bond. For V_N *h*-BN nanosheets, Fig. 1(c) shows its structure. The lattice constant is $a = b = 9.89$ Å, lattice angle $\alpha = \beta = 90°$ and $\gamma = 120°$, and bond length $d_{B\text{-}B} = 2.21$ Å. Compared with the V_B *h*-BN structure, the lattice constant of V_N *h*-BN nanosheets decreases. The number of B atoms in the V_N *h*-BN primitive cell is 16 and the number of N atoms is 15. There are charges localized at the N-vacancy, as shown in Fig. 1(d). The optimization results of all the

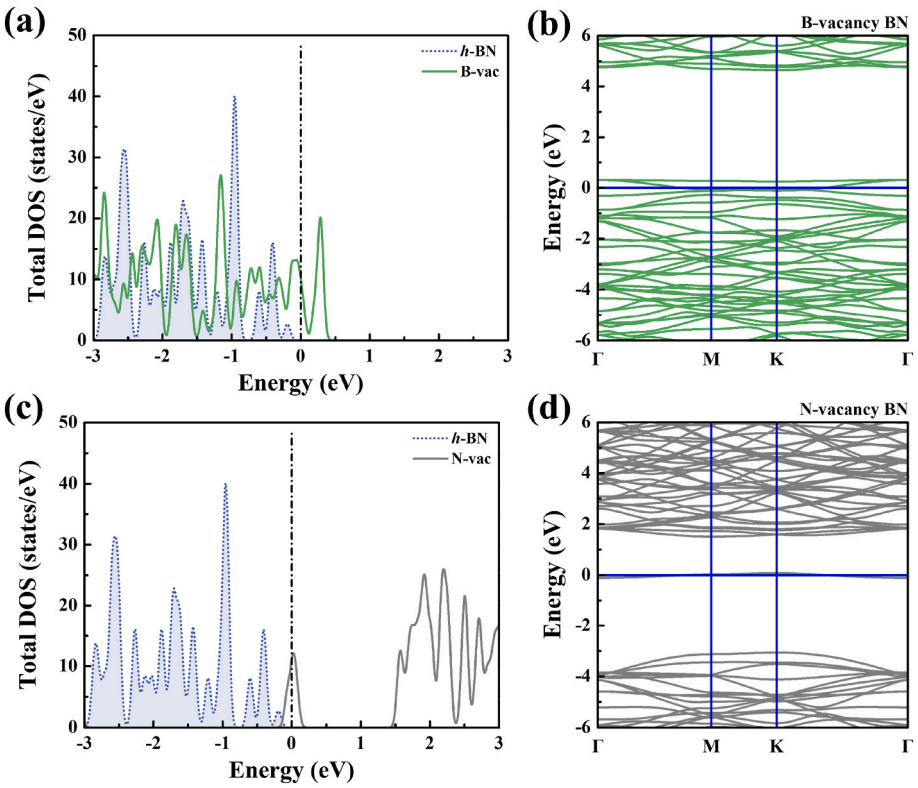

Fig. 2. The TDOS of (a) V_B *h*-BN nanosheets and (c) V_N *h*-BN nanosheets. The blue shaded area is the TDOS of intrinsic *h*-BN nanosheets. The band structure of (b) V_B *h*-BN nanosheets and (d) V_N *h*-BN nanosheets. (For interpretation of the references to colour in this figure legend, the reader is referred to the Web version of this article.)

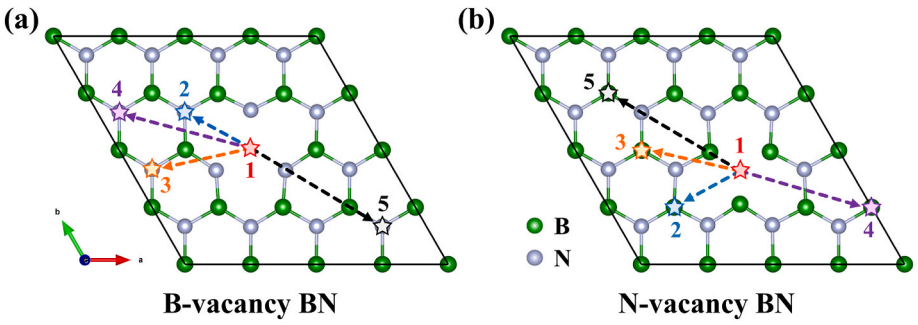

Fig. 3. Five typical adsorption sites on the (a) V_B *h*-BN nanosheets surface and (b) V_N *h*-BN nanosheets surface.

Table 2
After optimization, the adsorption energy E_{ad} (eV) of a single H atom on the V_B *h*-BN nanosheets and V_N *h*-BN nanosheets surface.

sample	site-1	site-2	site-3	site-4	site-5
B-vacancy	−5.23	−4.50	−4.28	−4.22	−4.14
N-vacancy	−3.30	−5.13	−5.24	−5.05	−5.07

architectures show that vacancy defects only lead to the reconstruction of B or N atoms in the *h*-BN plane. After reconstruction, all atoms are still in the same plane without longitudinal bending or folding, and V_B/V_N can still exist. In order to facilitate comparison with the structural parameters of intrinsic *h*-BN nanosheets, the structure of *h*-BN is also calculated, as shown in Fig. S1. For intrinsic *h*-BN nanosheets, the lattice constant is $a = b = 2.50$ Å, lattice angle $\alpha = \beta = 90°$ and $\gamma = 120°$, bond length $d_{B\text{-}B} = 2.50$ Å and $d_{N\text{-}N} = 2.50$ Å, which is in good agreement with other work [72]. It can prove the reliability of the calculation results. The structural parameters of *h*-BN nanosheets 4 × 4 × 1 supercell are listed in Table 1.

Based on the stable *h*-BN nanosheets with vacancy defects, we further studied their electronic properties, and calculated the total density of states (TDOS) and energy band structure of V_B and V_N *h*-BN nanosheets. In Fig. 2(a) and Fig. 2(c), the blue shaded area is the TDOS of intrinsic *h*-BN nanosheets. There is no distribution of electronic states at the Fermi-level, suggesting that *h*-BN is a wide band-gap semiconductor. The band gap of the *h*-BN is about 4.67 eV, as shown in Fig. S1(b). As for V_B and V_N *h*-BN nanosheets, it can be seen from their TDOS that there are electronic states passing through the Fermi-level and therefore both V_B and V_N *h*-BN nanosheets show metallic properties. Fig. 2(b) and (d) show the energy band structure of V_B and V_N *h*-BN, respectively.

3.2. Hydrogen absorption on the V_B and V_N *h*-BN nanosheets

The adsorption properties of hydrogen on the V_B and V_N *h*-BN nanosheets surface were investigated. For V_B *h*-BN nanosheets, by structural symmetry, a single hydrogen ion has five different adsorption sites at the V_B *h*-BN nanosheets surface, as shown in Fig. 3(a) and Fig. S2. In accordance with the definition of adsorption energy E_{ad} in Eq. (1), we calculated the E_{ad} of a single hydrogen ion at five adsorption sites, and the data are listed in Table 2. The E_{ad} data are negative, indicating that hydrogen ions can be stably adsorbed at these sites and on the V_B *h*-BN nanosheets surface. In Fig. 3(a), the hydrogen ion is mainly adsorbed on the top of the N atom. For V_N *h*-BN nanosheets, a single hydrogen ion also has five adsorption sites on its surface, as shown in Fig. 3(b). Unlike V_B *h*-BN, in V_N *h*-BN, the hydrogen ion is mainly and directly adsorbed above the B atom. And besides, the E_{ad} data are also negative. This means that for both B-vacancy and N-vacancy on the *h*-BN surface,

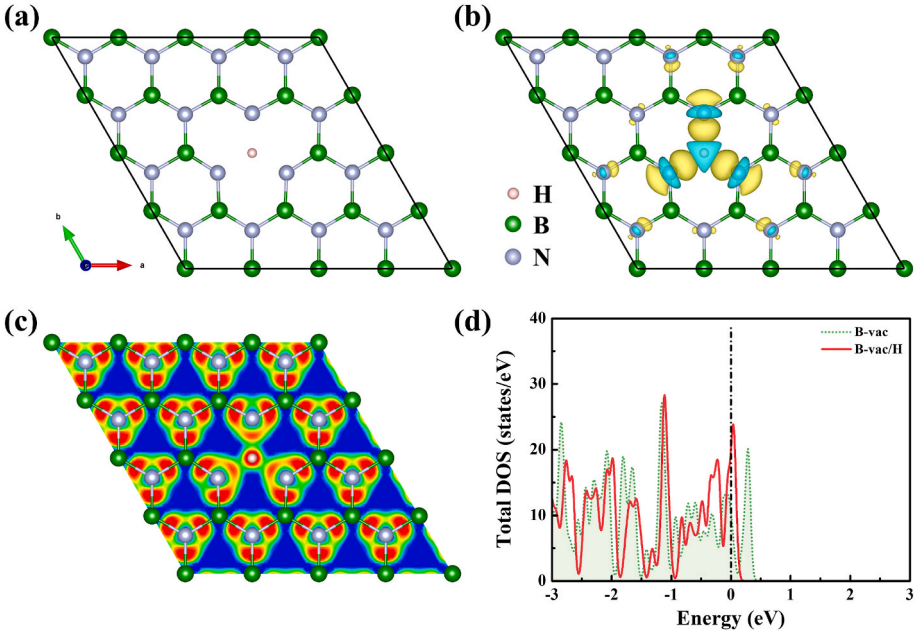

Fig. 4. (a) The structure of the H atom adsorbed at site-1 after optimization in V_B *h*-BN nanosheets. (b) The charge density difference of H/V_B *h*-BN system. (c) The sliced ELF map of the H/V_B *h*-BN system on the (001) crystal face. (d) The TDOS of the H/V_B *h*-BN system (red line). The green shaded area is the TDOS of V_B *h*-BN nanosheets. (For interpretation of the references to colour in this figure legend, the reader is referred to the Web version of this article.)

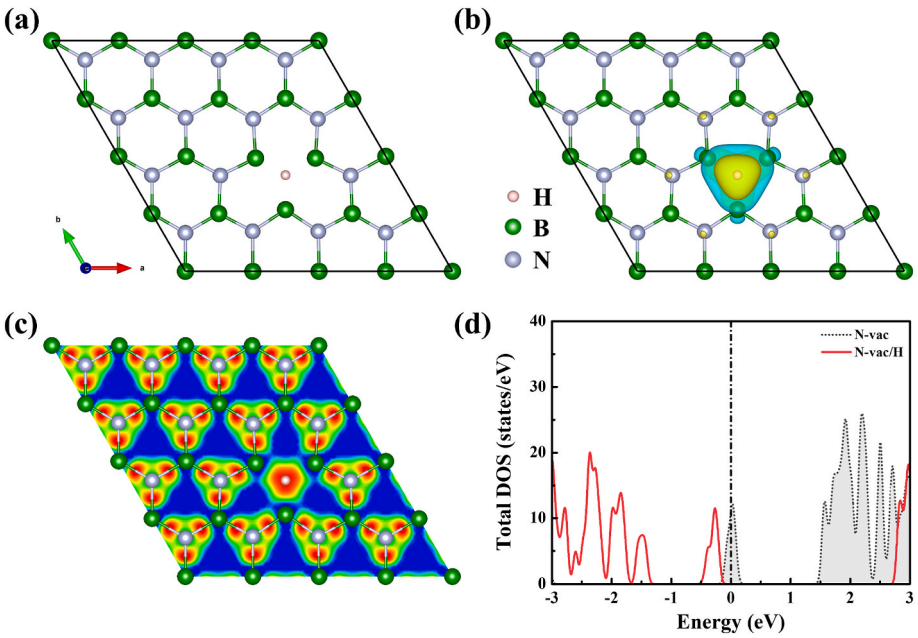

Fig. 5. (a) The structure of H atom adsorbed at site-1 after optimization in V_N *h*-BN nanosheets. (b) The charge density difference of H/V_N *h*-BN system. (c) The sliced ELF map of H/V_N *h*-BN system on the (001) crystal face. (d) The TDOS of H/V_N *h*-BN system (red line). The green shaded area is the TDOS of V_N *h*-BN nanosheets. (For interpretation of the references to colour in this figure legend, the reader is referred to the Web version of this article.)

hydrogen ion can spontaneously and stably adsorb on the surface of *h*-BN.

The adsorption behavior of single hydrogen on the V_B *h*-BN nanosheets surface was explored. There are many adsorption sites of hydrogen on the V_B *h*-BN surface, and a typical adsorption site was selected out: site-1, as the discussion object. A single hydrogen was placed at the B-vacancy as the initial adsorption position for structural optimization. The results showed that the hydrogen placed at the given initial position could not be automatically moved to other positions, and the structure did not deform after V_B *h*-BN adsorbed hydrogen, as shown in Fig. 4(a). Fig. 4(b) and (c) are the charge density difference and ELF map of a hydrogen ion adsorbed on the V_B *h*-BN nanosheets surface, respectively. As mentioned above, V_B *h*-BN nanosheets is metallic. When a single hydrogen ion is adsorbed on the V_B *h*-BN, the TDOS of H/V_B *h*-BN system is shown in Fig. 4(d). The red line is the TDOS of H/V_B *h*-BN system. The red line passes through the Fermi-level, which indicates that the H/V_B *h*-BN system is still metallic. See Fig. S3 to Fig. S6 four for other H/V_B *h*-BN systems.

For V_N *h*-BN nanosheets, the adsorption behavior of a single hydrogen ion at site-1 is discussed, and the four other H/V_N *h*-BN systems are shown in Fig. S7 to Fig. S10. In Fig. 5(a), the structure of a hydrogen atom adsorbed at site-1 after optimization in V_N *h*-BN nanosheets. And there is charge transfer between hydrogen ion and V_N *h*-BN nanosheets in the H/V_N *h*-BN system, as shown in Fig. 5(b), as well as the sliced ELF map of H/V_N *h*-BN system on the (001) crystal face is shown in Fig. 5(c). The E_{ad} is negative at site-1. These results show that hydrogen ion is chemisorpted on the V_N *h*-BN surface, which is the same as that of hydrogen ion on V_B *h*-BN surface. Additionally, when a single hydrogen ion is adsorbed on V_N *h*-BN surface, the system changes from metal to semiconductor, as shown in Fig. 5(d).

3.3. Hydrogen ion transport on the V_B and V_N *h*-BN nanosheets

As everyone knows, it is important and challenging to control the direction of ion transport at the atomic-level. In order to deeply understand the controllable factors, we studied the migration properties of hydrogen ions on the V_B and V_N *h*-BN nanosheets surface. In V_B *h*-BN nanosheets, according to the symmetry of the structure, a single hydrogen ion has seven different migration paths on its surface. To more clearly discuss the transport behavior of hydrogen ion, three paths were selected, as shown in Fig. 6(a). The path I is site-1 to site-2, the path II is site-3 to site-3, and the path III is site-3 to site-5. In Fig. 6(b), the migration barriers of a single hydrogen ion along path I, path II, and path III are 2.33 eV, 2.47 eV, and 1.83 eV, respectively. The migration of a single hydrogen ion along the other four paths is shown in Fig. S11.

In V_N *h*-BN nanosheets, we also selected three paths, as shown in

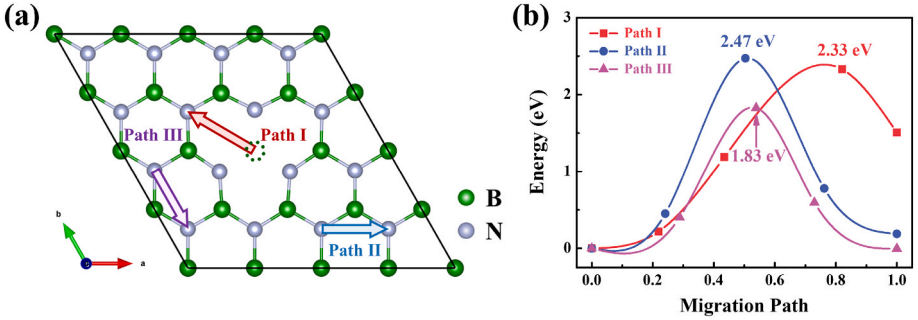

Fig. 6. (a) The hydrogen ion migration in Path I, Path II, and Path III on the V_B *h*-BN nanosheets surface. (b) The energy profile of hydrogen ion transport with different paths.

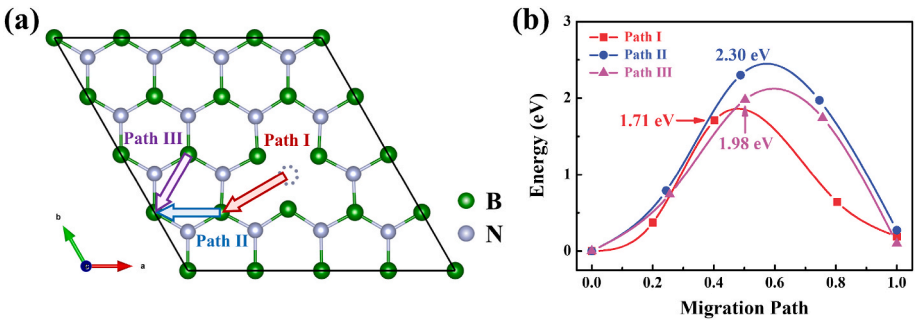

Fig. 7. (a) The hydrogen ion migration in Path I, Path II, and Path III on the V_N *h*-BN nanosheets surface. (b) The energy profile of hydrogen ion transport with different path.

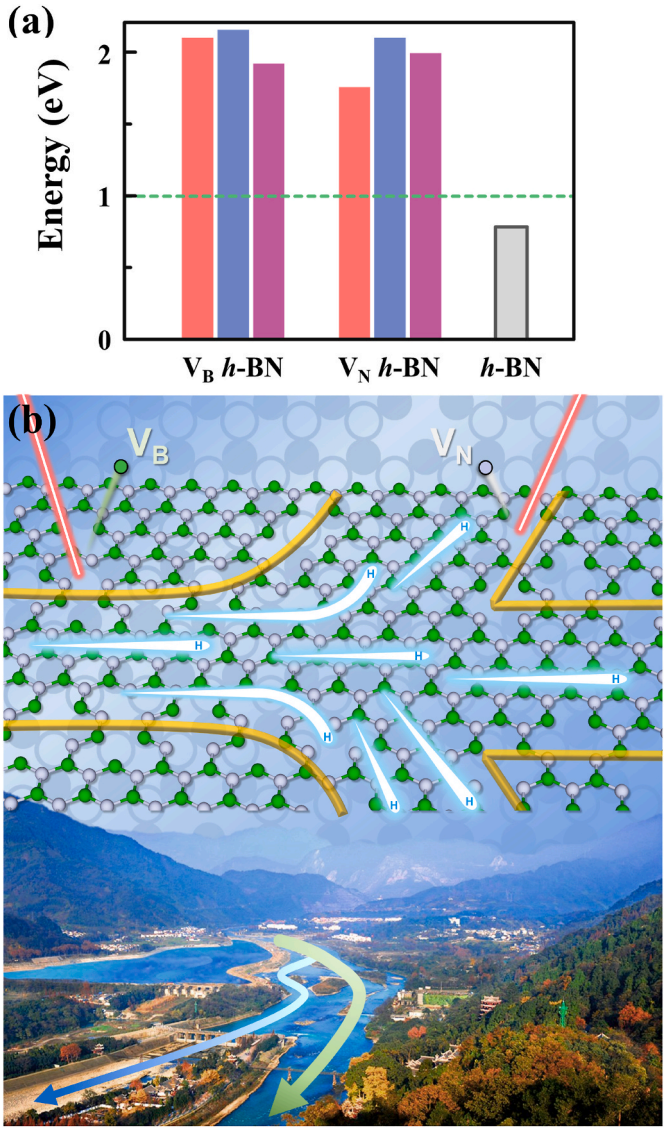

Fig. 8. (a) The migration energy of hydrogen ion in V_B, V_N, and intrinsic *h*-BN nanosheets. The green dotted line represents the threshold for hydrogen ion conduction. (b) Schematic diagram of vacancy-defect-induced atomic-level directional hydrogen ion conduction in *h*-BN nanosheets, which is similar to the world-famous Dujiangyan Irrigation Project [73]. (For interpretation of the references to colour in this figure legend, the reader is referred to the Web version of this article.)

Fig. 7(a). The path I is site-1 to site-2, the path II is site-2 to site-4, and the path III is site-3 to site-4. In Fig. 7(b), the migration barriers of a single hydrogen ion along path I, path II, and path III are 1.71 eV, 1.98 eV, and 2.30 eV, respectively. The migration barrier of hydrogen ion on the V_N *h*-BN surface is slightly lower than that on the V_B *h*-BN surface. The migration of a single hydrogen ion along the other four paths is shown in Fig. S12.

We have counted and summarized the migration barriers of hydrogen ion on the surfaces of V_B *h*-BN nanosheets, V_N *h*-BN nanosheets and intrinsic *h*-BN nanosheets, as shown in Fig. 8(a). The migration barriers of hydrogen ion on V_B *h*-BN and V_N *h*-BN surfaces are 1.83–2.47 eV and 1.71–2.30 eV, respectively. Moreover, the migration barrier of hydrogen ion on the intrinsic *h*-BN nanosheets surface is 0.72 eV (Fig. S13). In principle, the migration barrier of hydrogen ion in fast ionic conducting materials is no more than 1.0 eV [74,75], as shown in the green dotted line in Fig. 8(a). Obviously, the migration barriers of hydrogen ion for both V_B *h*-BN and V_N *h*-BN are much higher than this threshold value. This means that hydrogen ions can conduct in defect-free *h*-BN, while they cannot conduct in B/N-vacancy defects. Based on this, the femtosecond laser plasmonic lithography (FPL) [76] can be used to artificially construct vacancy defects with different directions and sizes on the *h*-BN nanosheets surface by using the accompanying nonlinear optical effect, which is similar to the principle of the oldest man-made water system in the world of the Dujiangyan Irrigation Project in China [73,77,78], as shown in Fig. 8(b). Directional control of water flow and/or hydrogen ion conduction using artificially constructed barriers. In this way, the conduction direction of hydrogen ion can be manually interfered by introducing man-made vacancies on the *h*-BN surface, and the atomic-level control of ion directional conduction can be realized in the *h*-BN nanosheets, being promising and working for ion-conductor integrated circuit and bioinspired nanofluidic iontronic devices [26,27].

4. Conclusion

Defect-engineered *h*-BN nanosheets as a vacancy-defect-controlled atomic-level directional hydrogen ion conductor was achieved, being promising for constructing new-type nanofluidic iontronic devices. The adsorption and migration behavior of hydrogen ion on the B-vacancy and N-vacancy *h*-BN nanosheets were systematically studied by the first-principle method. It is found that the migration barrier of hydrogen ions is 1.83–2.47 eV on the surface of B-vacancy *h*-BN and 1.71–2.30 eV on the surface of N-vacancy *h*-BN, much higher than the threshold value of 1.0 eV, while the migration barrier of hydrogen ion on the intrinsic *h*-BN surface is only 0.72 eV. Accordingly, hydrogen ion conduction in *h*-BN can be directionally controlled by controlling the position of vacancy defects, which can be artificially constructed through femtosecond laser plasma lithography. This work provides a new technology of vacancy-defect-induced atomic-level directional ions conduction in 2D materials for ion-conductor integrated circuit, which is a new strategy to

realize atomic-level artificially controlled ion directional conduction in flexible iontronics. Additionally, it opens the door for constructing bioinspired nanofluidic iontronic devices in future neuronal-computer interfaces.

Declaration of competing interest

The authors declare that they have no known competing financial interests or personal relationships that could have appeared to influence the work reported in this paper.

Acknowledgments

This work was supported by the Ministry of Science and Technology of China (No. 2021YFE0100200), Pakistan Science Foundation (PSF) Project (No. PSF/CRP/18thProtocol (01)), the Science and Technology Department of Sichuan Province (No. 2023YFG0202), the Fundamental Research Funds for the Central Universities of the University of Electronic Science and Technology of China (A03018023601020, ZYGX2021J011) and the National Natural Science Foundation of China (Grants No. 12064015).

Appendix A. Supplementary data

Supplementary data to this article can be found online at https://doi.org/10.1016/j.ceramint.2023.04.171.

References

[1] C.K. Chan, H. Peng, G. Liu, K. McIlwrath, X.F. Zhang, R.A. Huggins, Y. Cui, High-performance lithium battery anodes using silicon nanowires, Nat. Nanotechnol. 3 (2008) 31–35.
[2] V. Augustyn, J. Come, M.A. Lowe, J.W. Kim, P.-L. Taberna, S.H. Tolbert, H. D. Abruna, P. Simon, B. Dunn, High-rate electrochemical energy storage through Li^+ intercalation pseudocapacitance, Nat. Mater. 12 (2013) 518–522.
[3] Y. Xia, T.S. Mathis, M.-Q. Zhao, B. Anasori, A. Dang, Z. Zhou, H. Cho, Y. Gogotsi, S. Yang, Thickness-independent capacitance of vertically aligned liquid-crystalline MXenes, Nature 557 (2018) 409.
[4] E. Shi, B. Yuan, S.B. Shiring, Y. Gao, Akriti, Y. Guo, C. Su, M. Lai, P. Yang, J. Kong, B.M. Savoie, Y. Yu, L. Dou, Two-dimensional halide perovskite lateral epitaxial heterostructures, Nature 580 (2020) 614.
[5] L. Wang, G. Gao, Y. Zhou, T. Xu, J. Chen, R. Wang, R. Zhang, J. Fu, Tough, Adhesive, self-healable, and transparent ionically conductive zwitterionic nanocomposite hydrogels as skin strain sensors, ACS Appl. Mater. Interfaces 11 (2019) 3506–3515.
[6] T. Li, L. Li, H. Sun, Y. Xu, X. Wang, H. Luo, Z. Liu, T. Zhang, Porous ionic membrane based flexible humidity sensor and its multifunctional applications, Adv. Sci. 4 (2017).
[7] G. Korotcenkov, S. Do Han, J.R. Stetter, Review of electrochemical hydrogen sensors, Chem. Rev. 109 (2009) 1402–1433.
[8] J. Yu, Y. Feng, D. Sun, W. Ren, C. Shao, R. Sun, Highly conductive and mechanically robust cellulose nanocomposite hydrogels with antifreezing and antidehydration performances for flexible humidity sensors, ACS Appl. Mater. Interfaces 14 (2022) 10886–10897.
[9] D. Lei, Q. Zhang, N. Liu, T. Su, L. Wang, Z. Ren, Y. Gao, An ion channel-induced self-powered flexible pressure sensor based on potentiometric transduction mechanism, Adv. Funct. Mater. 32 (2022).
[10] H. Wu, H. Jia, C. Wang, J.-G. Zhang, W. Xu, Recent progress in understanding solid electrolyte interphase on lithium metal anodes, Adv. Energy Mater. 11 (2021).
[11] Z.Q. Wang, H.Y. Xu, X.H. Li, H. Yu, Y.C. Liu, X.J. Zhu, Synaptic learning and memory functions achieved using oxygen ion migration/diffusion in an amorphous InGaZnO memristor, Adv. Funct. Mater. 22 (2012) 2759–2765.
[12] S. Song, X. Xiong, X. Wu, Z. Xue, Modeling the SOFC by BP neural network algorithm, Int. J. Hydrogen Energy 46 (2021) 20065–20077.
[13] Y. Cao, T. Zhao, C. Zhao, Y. Liu, P. Song, H. Gao, C.Z. Zhao, Advanced artificial synaptic thin-film transistor based on doped potassium ions for neuromorphic computing via third-generation neural network, J. Mater. Chem. C 10 (2022) 3196–3206.
[14] W. Nernst, Ueber das chemische Gleichgewicht, elektromotorische Wirksamkeit und elektrolytische Abscheidung von Metallgemischen, Z. Phys. Chem. 22U (1897) 539–542.
[15] H. Iwahara, T. Esaka, H. Uchida, N. Maeda, Proton conduction in sintered oxides and its application to steam electrolysis for hydrogen production, Solid State Ionics 3–4 (1981) 359–363.
[16] J.B. Goodenough, B. John, Goodenough-Facts-2019, NobelPrize.org, 2019.
[17] K. Mizushima, P.C. Jones, P.J. Wiseman, J.B. Goodenough, Li_xCoO_2 (0<x<-1): a new cathode material for batteries of high energy density, Mater. Res. Bull. 15 (1980) 783–789.
[18] T. Huebert, L. Boon-Brett, G. Black, U. Banach, Hydrogen sensors-A review, Sensor. Actuator. B Chem. 157 (2011) 329–352.
[19] F. Favier, E.C. Walter, M.P. Zach, T. Benter, R.M. Penner, Hydrogen sensors and switches from electrodeposited palladium mesowire arrays, Science 293 (2001) 2227–2231.
[20] G. Li, Y. Shen, S. Zhao, A. Li, S. Gao, D. Wei, Z. Yuan, F. Meng, D. Meng, High response and moisture resistance hydrogen sensors based on sandwich-structured PtSnx-rGO-SnO_2 nanocomposites, Sensor. Actuator. B Chem. 368 (2022).
[21] Z. Zhi, W. Gao, J. Yang, C. Geng, B. Yang, C. Tian, S. Fan, H. Li, J. Li, Z. Hua, Amperometric hydrogen gas sensor based on Pt/C/Nafion electrode and ionic electrolyte, Sensor. Actuator. B Chem. 367 (2022).
[22] J.J. Yang, M.D. Pickett, X. Li, D.A.A. Ohlberg, D.R. Stewart, R.S. Williams, Memristive switching mechanism for metal/oxide/metal nanodevices, Nat. Nanotechnol. 3 (2008) 429–433.
[23] J.J. Yang, D.B. Strukov, D.R. Stewart, Memristive devices for computing, Nat. Nanotechnol. 8 (2013) 13–24.
[24] M. Prezioso, F. Merrikh-Bayat, B.D. Hoskins, G.C. Adam, K.K. Likharev, D. B. Strukov, Training andoperation of an integrated neuromorphic network based on metal-oxide memristors, Nature 521 (2015) 61–64.
[25] Z.-H. Tan, R. Yang, K. Terabe, X.-B. Yin, X.-D. Zhang, X. Guo, Synaptic metaplasticity realized in oxide memristive devices, Adv. Mater. 28 (2016) 377–384.
[26] Y. Hou, X. Hou, Bioinspired nanofluidic iontronics, Science 373 (2021) 628–629.
[27] P. Robin, N. Kavokine, L. Bocquet, Modeling of emergent memory and voltage spiking in ionic transport through angstrom-scale slits, Science 373 (2021) 687–691.
[28] J. Jiang, Y. Zhang, P. Nie, G. Xu, M. Shi, J. Wang, Y. Wu, R. Fu, H. Dou, X. Zhang, Progress of nanostructured electrode materials for supercapacitors, Adv. Sustain. Syst. 2 (2018).
[29] Y. Ai, Y. You, F. Wei, X. Jiang, Z. Han, J. Cui, H. Luo, Y. Li, Z. Xu, S. Xu, J. Yang, Q. Bao, C. Jing, J. Fu, J. Cheng, S. Liu, Hollow bio-derived polymer nanospheres with ordered mesopores for sodium-ion battery, Nano-Micro Lett. 12 (2020).
[30] Y. Sun, Y. Wang, X. Liang, Y. Xia, L. Peng, H. Jia, H. Li, L. Bai, J. Feng, H. Jiang, J. Xie, Rotational cluster anion enabling superionic conductivity in sodium-rich antiperovskite Na_3OBH_4, J. Am. Chem. Soc. 141 (2019) 5640–5644.
[31] X. Zhu, X. Hu, S. Yan, Y. Peng, W. Feng, D. Guo, Y. Gao, S. Zhang, A. Cassimi, J. Xu, D. Zhao, D. Dong, B. Hai, Y. Wu, J. Wang, X. Ma, Heavy N^+ ion transfer in doubly charged N_2Ar van der Waals cluster, Nat. Commun. 11 (2020).
[32] S. Iijima, Helical microtubules of graphitic carbon, Nature 354 (1991) 56–58.
[33] D. Liu, X. Huang, D. Qu, D. Zheng, G. Wang, J. Harris, J. Si, T. Ding, J. Chen, D. Qu, Confined phosphorus in carbon nanotube-backboned mesoporous carbon as superior anode material for sodium/potassium-ion batteries, Nano Energy 52 (2018) 1–10.
[34] C.Y. Won, N.R. Aluru, A chloride ion-selective boron nitride nanotube, Chem. Phys. Lett. 478 (2009) 185–190.
[35] A.K. Geim, K.S. Novoselov, The rise of graphene, Nat. Mater. 6 (2007) 183–191.
[36] A. Splendiani, L. Sun, Y. Zhang, T. Li, J. Kim, C.-Y. Chim, G. Galli, F. Wang, Emerging photoluminescence in monolayer MoS_2, Nano Lett. 10 (2010) 1271–1275.
[37] E. Yoo, J. Kim, E. Hosono, H.-s. Zhou, T. Kudo, I. Honma, Large reversible Li storage of graphene nanosheet families for use in rechargeable lithium ion batteries, Nano Lett. 8 (2008) 2277–2282.
[38] K. Hatakeyama, M.S. Islam, K. Michio, C. Ogata, T. Taniguchi, A. Funatsu, T. Kida, S. Hayami, Y. Matsumoto, Super proton/electron mixed conduction in graphene oxide hybrids by intercalating sulfate ions, J. Mater. Chem. 3 (2015) 20892–20895.
[39] S. Chabi, C. Peng, D. Hu, Y. Zhu, Ideal three-dimensional electrode structures for electrochemical energy storage, Adv. Mater. 26 (2014) 2440–2445.
[40] J. Xu, X. Wang, X. Wang, D. Chen, X. Chen, D. Li, G. Shen, Three-dimensional structural engineering for energy-storage devices: from microscope to macroscope, Chemelectrochem 1 (2014) 975–1002.
[41] K.D. Kreuer, Proton-conducting oxides, Annu. Rev. Mater. Res. 33 (2003) 333–359.
[42] N. Kamaya, K. Homma, Y. Yamakawa, M. Hirayama, R. Kanno, M. Yonemura, T. Kamiyama, Y. Kato, S. Hama, K. Kawamoto, A. Mitsui, A lithium superionic conductor, Nat. Mater. 10 (2011) 682–686.
[43] C. Eames, J.M. Frost, P.R.F. Barnes, B.C. O'Regan, A. Walsh, M.S. Islam, Ionic transport in hybrid lead iodide perovskite solar cells, Nat. Commun. 6 (2015).
[44] J.C. Bachman, S. Muy, A. Grimaud, H.-H. Chang, N. Pour, S.F. Lux, O. Paschos, F. Maglia, S. Lupart, P. Lamp, L. Giordano, Y. Shao-Horn, Inorganic solid-state electrolytes for lithium batteries: mechanisms and properties governing ion conduction, Chem. Rev. 116 (2016) 140–162.
[45] Y. Chen, Z. Wang, X. Li, X. Yao, C. Wang, Y. Li, W. Xue, D. Yu, S.Y. Kim, F. Yang, A. Kushima, G. Zhang, H. Huang, N. Wu, Y.-W. Mai, J.B. Goodenough, J. Li, Li metal deposition and stripping in a solid-state battery via Coble creep, Nature 578 (2020) 251.
[46] C. Yang, Q. Wu, W. Xie, X. Zhang, A. Brozena, J. Zheng, M.N. Garaga, B.H. Ko, Y. Mao, S. He, Y. Gao, P. Wang, M. Tyagi, F. Jiao, R. Briber, P. Albertus, C. Wang, S. Greenbaum, Y.-Y. Hu, A. Isogai, M. Winter, K. Xu, Y. Qi, L. Hu, Copper-coordinated cellulose ion conductors for solid-state batteries, Nature 598 (2021) 590.
[47] Y. Kubota, K. Watanabe, O. Tsuda, T. Taniguchi, Deep ultraviolet light-emitting hexagonal boron nitride synthesized at atmospheric pressure, Science 317 (2007) 932–934.

[48] C. Zhi, Y. Bando, C. Tang, H. Kuwahara, D. Golberg, Large-scale fabrication of boron nitride nanosheets and their utilization in polymeric composites with improved thermal and mechanical properties, Adv. Mater. 21 (2009) 2889–2893.
[49] Z. Lin, A. McNamara, Y. Liu, K.-s. Moon, C.-P. Wong, Exfoliated hexagonal boron nitride-based polymer nanocomposite with enhanced thermal conductivity for electronic encapsulation, Compos. Sci. Technol. 90 (2014) 123–128.
[50] X. Duan, Z. Yang, L. Chen, Z. Tian, D. Cai, Y. Wang, D. Jia, Y. Zhou, Review on the properties of hexagonal boron nitride matrix composite ceramics, J. Eur. Ceram. Soc. 36 (2016) 3725–3737.
[51] L. Song, L. Ci, H. Lu, P.B. Sorokin, C. Jin, J. Ni, A.G. Kvashnin, D.G. Kvashnin, J. Lou, B.I. Yakobson, P.M. Ajayan, Large scale growth and characterization of atomic hexagonal boron nitride layers, Nano Lett. 10 (2010) 3209–3215.
[52] S. Hu, M. Lozada-Hidalgo, F.C. Wang, A. Mishchenko, F. Schedin, R.R. Nair, E. W. Hill, D.W. Boukhvalov, M.I. Katsnelson, R.A.W. Dryfe, I.V. Grigorieva, H.A. Wu, A.K. Geim, Proton transport through one-atom-thick crystals, Nature 516 (2014) 227–230.
[53] C. Chen, G. Wang, B. Admasu Beshiwork, B. Xu, B. Lin, Strain-tunable pure H^- conduction in one-atom-thick hexagonal boron nitride for high-energy-density fuel cells, Chem. Eng. J. 450 (2022), 138223.
[54] N. Alem, R. Erni, C. Kisielowski, M.D. Rossell, W. Gannett, A. Zettl, Atomically thin hexagonal boron nitride probed by ultrahigh-resolution transmission electron microscopy, Phys. Rev. B 80 (2009), 155425.
[55] C. Jin, F. Lin, K. Suenaga, S. Iijima, Fabrication of a freestanding boron nitride single layer and its defect assignments, Phys. Rev. Lett. 102 (2009), 195505.
[56] Y. Xiao, H. Yu, H. Wang, X. Zhu, L. Chen, W. Gao, C. Liu, H. Yin, Defect engineering of hexagonal boron nitride nanosheets via hydrogen plasma irradiation, Appl. Surf. Sci. 593 (2022), 153386.
[57] Q. Peng, J. Crean, A.K. Dearden, C. Huang, X. Wen, S.P.A. Bordas, S. De, Defect engineering of 2D monatomic-layer materials, Mod. Phys. Lett. B 27 (2013).
[58] Y. Zhang, Y.-F. Yao, Y.-Y. Qiao, G.-C. Wang, First-principles theoretical study on dry reforming of methane over perfect and boron-vacancy-containing *h*-BN sheet-supported Ni catalysts, Phys. Chem. Chem. Phys. 23 (2021) 617–627.
[59] Y. Shen, S. Zhu, Machine learning mechanical properties of defect-engineered hexagonal boron nitride, Comput. Mater. Sci. 220 (2023).
[60] A.I. Liechtenstein, V.I. Anisimov, J. Zaanen, Density-functional theory and strong interactions: orbital ordering in Mott-Hubbard insulators, Phys. Rev. B 52 (1995) R5467–R5470.
[61] D. Neuhauser, R. Baer, E. Rabani, Communication: embedded fragment stochastic density functional theory, J. Chem. Phys. 141 (2014).
[62] G. Kresse, J. Hafner, Ab initio molecular-dynamics simulation of the liquid-metal-amorphous-semiconductor transition in germanium, Phys. Rev. B 49 (1994) 14251–14269.
[63] G. Kresse, J. Furthmüller, Efficient iterative schemes for ab initio total-energy calculations using a plane-wave basis set, Phys. Rev. B 54 (1996), 11169.
[64] G. Kresse, J. Furthmuller, Efficiency of ab-initio total energy calculations for metals and semiconductors using a plane-wave basis set, Comput. Mater. Sci. 6 (1996) 15–50.
[65] P.E. Blöchl, Projector augmented-wave method, Phys. Rev. B 50 (1994), 17953.
[66] P. Jp, B. K, E. M, Generalized gradient approximation made simple, Phys. Rev. Lett. 77 (1998) 3865–3868.
[67] H.J. Monkhorst, J.D. Pack, Special points for Brillouin-zone integrations, Phys. Rev. B 13 (1976) 5188.
[68] S. Grimme, Semiempirical GGA-type density functional constructed with a long-range dispersion correction, J. Comput. Chem. 27 (2006) 1787–1799.
[69] S. Grimme, J. Antony, S. Ehrlich, H. Krieg, A consistent and accurate ab initio parametrization of density functional dispersion correction (DFT-D) for the 94 elements H-Pu, J. Chem. Phys. 132 (2010), 154104.
[70] G. Henkelman, B.P. Uberuaga, H. Jonsson, A climbing image nudged elastic band method for finding saddle points and minimum energy paths, J. Chem. Phys. 113 (2000) 9901–9904.
[71] K. Momma, F. Izumi, VESTA: a three-dimensional visualization system for electronic and structural analysis, J. Appl. Crystallogr. 41 (2008) 653–658.
[72] L. Shi, A. Xu, T. Zhao, First-principles investigations of the working mechanism of 2D *h*-BN as an interfacial layer for the anode of lithium metal batteries, ACS Appl. Mater. Interfaces 9 (2017) 1987–1994.
[73] Dujiangyan Irrigation Project Municipal People's Government, 2023.
[74] H.W.T. Morgan, H.J. Stroud, N.L. Allan, Improving hydride conductivity in layered perovskites via crystal engineering, Chem. Mater. 33 (2021) 177–185.
[75] K. Fukui, S. Iimura, T. Tada, S. Fujitsu, M. Sasase, H. Tamatsukuri, T. Honda, K. Ikeda, T. Otomo, H. Hosono, Characteristic fast H^- ion conduction in oxygen-substituted lanthanum hydride, Nat. Commun. 10 (2019).
[76] T. Zou, B. Zhao, W. Xin, Y. Wang, B. Wang, X. Zheng, H. Xie, Z. Zhang, J. Yang, C. Guo, High-speed femtosecond laser plasmonic lithography and reduction of graphene oxide for anisotropic photoresponse, Light Sci. Appl. 9 (2020) 69.
[77] S. Zhang, Y. Yi, Y. Liu, X. Wang, Hydraulic principles of the 2,268-year-old dujiangyan Project in China, J. Hydraul. Eng. 139 (2013) 538–546.
[78] M. Huang, C. Zhu, C. Ma, Z. Yang, Y. Liu, T. Jia, The Hongqiaocun Site: the earliest evidence of ancient flood sedimentation of the water conservancy facilities in the Chengdu Plain, China, Catena (2020) 185.